ACS APPLIED MATERIALS & INTERFACES

Research Article

www.acsami.org

Tube-Like Ternary α-Fe_2O_3@SnO_2@Cu_2O Sandwich Heterostructures: Synthesis and Enhanced Photocatalytic Properties

Qingyong Tian,[†,‡] Wei Wu,*[,‡,§] Lingling Sun,[†] Shuanglei Yang,[∥] Mei Lei,[†] Juan Zhou,[†] Ying Liu,[†] Xiangheng Xiao,[†] Feng Ren,*[,†] Changzhong Jiang,[†] and Vellaisamy A. L. Roy*[,§]

[†]Key Laboratory of Artificial Micro- and Nano-structures of Ministry of Education, School of Physics and Technology, Wuhan University, Wuhan, Hubei 430072, P. R. China

[‡]Laboratory of Printable Functional Nanomaterials and Printed Electronics, School of Printing and Packaging, Wuhan University, Wuhan, Hubei 430072, P. R. China

[§]Department of Physics and Materials Science and Center of Super Diamond and Advanced Films (COSDAF), City University of Hong Kong, Kowloon Tong, Hong Kong, SAR, P. R. China

[∥]State Key Laboratory for Powder Metallurgy, Central South University, Changsha, Hunan 410083, P. R. China

Supporting Information

ABSTRACT: Heterogeneous photocatalysis is of great interest for environmental remediation applications. However, fast recombination of photogenerated electron−hole pair and a low utilization rate of sunlight hinder the commercialization of currently available semiconductor photocatalysts. In this regard, we developed a unique ternary single core-double shell heterostructure that consists of α-Fe_2O_3@SnO_2@Cu_2O. This heterostructure exhibits a tube-like morphology possessing broad spectral response for the sunlight due to the combination of narrow bandgap and wide bandgap semiconductors forming a p−n heterojunction. To fabricate such a short nanotube (SNT), we used an anion-assisted hydrothermal route for deposition of α-Fe_2O_3, a seed-mediated deposition strategy for SnO_2, and finally an aging process to deposit a Cu_2O layer to complete the tube-like ternary α-Fe_2O_3@SnO_2@Cu_2O single core-double shell heterostructures. The morphology, composition, and photocatalytic properties of those ternary core−shell−shell heterostructures were characterized by various analytical techniques. These ternary heterostructures exhibited enhanced photocatalytic properties on the photodegradation of the organic dye of Rhodamine B (RhB) under simulated sunlight irradiation. The origin of enhanced photocatalytic activity is due to the synergistic effect of broad spectral response by combining narrow bandgap and wide bandgap semiconductors and, hence, an efficient charge separation of photogenerated electron−hole pairs facilitated through the p−n heterojunction. Furthermore, our unique structure provides an insight on the fabrication and controlled preparation of multilayer heterostructural photocatalysts that have intriguing properties.

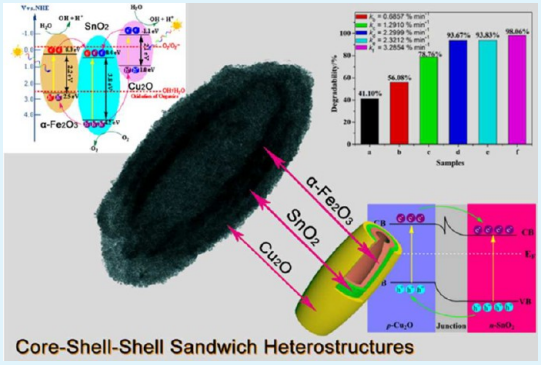

KEYWORDS: *iron oxide, multilayer heterostructure, p−n heterojunction, photocatalytic activity*

INTRODUCTION

The core−shell structural nanomaterials have attracted considerable attention in nanotechnology due to their improved physical and chemical properties.[1] A nanomaterial with a core−shell architecture is a feasible way to combine multiple functionalities on a nanoscopic length scale.[2] Recently, various core−shell heterostructural semiconductor nanomaterials have been used in photocatalytic application.[3−5] From the viewpoint of the photocatalysis application, an efficient charge separation mechanism involves, in both a capped semiconductor system and a coupled semiconductor system, the photogenerated electrons in one semiconductor being injected into the lower lying conduction band of the second semiconductor. Therefore, the core−shell heterostructure displays enhanced photocatalytic abilities when combining two semiconductors with a narrow and wide bandgap, such as α-Fe_2O_3@TiO_2, CdS@TiO_2, α-Fe_2O_3@SnO_2, α-Fe_2O_3@ZnO, Bi_2O_3@Bi_2WO_6, etc.[6−17] In such a photocatalytic system, the electronic structure of the wide bandgap semiconductor and the narrow bandgap semiconductor plays an important role. The narrow bandgap semiconductor should have a higher conduction band minimum and valence band maximum compared to the wide bandgap semiconductor, for the smooth injection of electrons downhill from the conduction band of the narrow bandgap semiconductor and the transfer of holes uphill to the valence band of the narrow bandgap semiconductor.[18] The main idea of the above heterostructuring procedure is to isolate the oxidation reaction due to holes and the reduction

Received: May 14, 2014
Accepted: July 3, 2014
Published: July 3, 2014

   dx.doi.org/10.1021/am5029439 | ACS Appl. Mater. Interfaces 2014, 6, 13088−13097

reaction due to electrons at two different sites, in order to prevent the charge carrier recombination. Moreover, the incorporation of small band gap semiconductors increases the probability of light absorption in the visible range.

In addition, the separation of photoinduced hole−electron pairs can be accelerated by the potential difference at the p−n heterojunction interface; hence, an obvious enhancement in photocatalytic performance is anticipated. It is known that surface potential has a gradient at the junction due to the diffusion of charge carriers (hole and/or electrons) on the surface of photocatalyst with the p−n junction structure. The difference in the surface potential is expected to create spatially separated oxidation and reduction sites on the surface[19] and building of an internal electric field with its field direction from the n-type to the p-type semiconductor.[20] Recently, various p−n semiconductor heterojunctions have been used for photocatalytic applications.[21−23] For example, Ganguli and coworkers have fabricated a type-II semiconductor with a p−n heterojunction by decorating a CuS nanostructure on the surface of ZnO nanotubes with the help of a wet-chemical method at low temperature. These ZnO/CuS heterostructures efficiently decomposed methylene blue upon irradiation of visible light at room temperature and displayed an enhanced visible light photocatalytic efficiency.[24]

There have been few studies on the design and controllable synthesis of composite heterostructures combining narrow/wide bandgap core−shell heterostructure with p−n heterojunction for photocatalytic application. Here, we report for the first time a tube-like ternary α-Fe_2O_3@SnO_2@Cu_2O single core-double shell sandwich heterostructure through controllable synthesis. Regarding the hybrid system, three kinds of important semiconductors such as α-Fe_2O_3, SnO_2, and Cu_2O have increasingly gained attention over the past decade. The α-Fe_2O_3 (E_g = 2.2 eV) and SnO_2 (E_g = 3.6 eV) are the n-type semiconductors; Cu_2O (E_g = 2.2 eV) is a p-type semiconductor. The α-Fe_2O_3 and SnO_2 form a core−shell heterostructure with a narrow/wide bandgap. The Cu_2O possesses high hole concentration, high hole mobility, and low lattice mismatch with SnO_2, which is beneficial for the formation of the p−n heterojunction with SnO_2. Finally, a heterostructure with a narrow-wide bandgap composite and p−n heterojunction system has been formed with enhanced photocatalytic abilities superior to pure α-Fe_2O_3 short nanotubes (SNTs) and binary α-Fe_2O_3/SnO_2 core−shell SNTs. Furthermore, we discuss the photocatalytic mechanism of the ternary core−shell−shell sandwich heterostructures. The results provide a useful insight into the design and interface of the core−shell heterostructures for photocatalytic applications.

EXPERIMENTAL SECTION

Materials and Chemicals. Ferric chloride hexahydrate ($FeCl_3·6H_2O$), anhydrous sodium sulfate (Na_2SO_4), sodium dihydrogen phosphate ($NaH_2PO_4·2H_2O$), copper(II) chloride dihydrate ($CuCl_2·2H_2O$), urea ($CO(NH_2)_2$), sodium dodecyl sulfate ($NaC_{12}H_{25}SO$, SDS), and ethanol (C_2H_5OH) were purchased from Sinopharm Chemical Reagent Co., Ltd. Potassium stannate trihydrate ($K_2SnO_3·3H_2O$), sodium hydroxide (NaOH), hydroxylamine hydrochloride ($NH_2OH·HCl$), and Rhodamine B (RhB) were purchased from Shanghai Aladdin Reagents Co., Ltd. All the reagents were analytically pure (AR) and used as received without further purification. The deionized water was used throughout the experiments.

Synthesis of α-Fe_2O_3 SNTs. According to our previous report, monodisperse α-Fe_2O_3 SNTs were prepared by using an anion-assisted hydrothermal route.[25,26] In a typical procedure, 0.27 g of $FeCl_3·6H_2O$, 7 mg of NaH_2PO_4, and 19.5 mg of Na_2SO_4 were dissolved into 25 mL of deionized water in a flask. Then, the mixture solution was transferred to a 30 mL Teflon-lined stainless steel autoclave, and the autoclave was sealed and heated at 220 °C for 12 h and then cooled down to room temperature naturally. The obtained α-Fe_2O_3 SNTs were washed several times with ethanol and deionized water before drying under vacuum at 60 °C for 12 h.

Synthesis of α-Fe_2O_3@SnO_2 Core−Shell SNTs. For the synthesis of α-Fe_2O_3@SnO_2 core−shell SNTs, 20 mg of as-generated α-Fe_2O_3 SNTs were dispersed in a mixed solvent consisting of 15.625 mL of deionized water and 9.625 mL of absolute alcohol. The urea and potassium stannate was mixed at a mass ratio of 5:1 under vigorous stirring for 10 min. Then, the mixture solution was transferred to a 50 mL Teflon-lined stainless steel autoclave and heated at 170 °C for 16 h and then cooled down to room temperature naturally. The as-prepared α-Fe_2O_3@SnO_2 SNTs were centrifuged and washed several times with ethanol and deionized water before drying under vacuum at 60 °C for 12 h.

Synthesis of α-Fe_2O_3@SnO_2@Cu_2O single core-double shell SNTs. Subsequently, the α-Fe_2O_3@SnO_2@Cu_2O core−shell−shell SNTs were prepared by means of an aging process. In a typical synthesis, 5 mg of as-obtained Fe_2O_3@SnO_2 SNTs and 0.087g of SDS (sodium dodecyl sulfate) were dissolved into 9.4 mL of deionized water under ultrasonification. Then, a certain amount of $CuCl_2$ solution, 0.25 mL of 1 M NaOH, and 0.25 mL of 0.2 M $NH_2OH·HCl$ were added into the above mixture in this order. The volume of as-added $CuCl_2$ aqueous solution was 0.1 mL, and the controlling parameter of concentration was varied, including 1, 50, and 100 mM, in order to adjust and obtain a Cu_2O layer with different thicknesses. The total volume of the mixture is kept at 10 mL, and then, the aging process follows for 2 h. After the reaction, all the solutions were washed with deionized water for four times and centrifuged at 3000 rpm for 5 min to remove the SDS. Finally, the precipitate was dispersed in 0.5 mL of ethanol for further characterization.

Characterization. Field emission scanning electron microscopy (FSEM) studies were carried out using a FEI Nova 400 NanoSEM operated at 20 keV. Transmission electron microscopy (TEM) characterization was carried out by a JEOL JEM-2010 (HT) operated at 200 kV. High-resolution TEM (HRTEM) images and energy-dispersive X-ray spectroscopy (EDX) were performed on a JEOL JEM-2100F transmission electron microscope at 200 kV. The samples were dissolved in water and dropped on carbon covered copper grids for inspection. Powder X-ray diffraction (XRD) patterns were recorded on a D/ruax2550PC (Japan) using Cu Kα radiation (λ = 0.1542 nm) operated at 40 kV and 40 mA at a scan rate of 0.05° 2θ S^{-1}. X-ray photoelectron spectroscopy (XPS) analysis was performed on a Thermo Scientific ESCALAB 250Xi system with Al Kα (1486.6 eV) as the radiation source.

Photocatalytic Tests. The photocatalytic performance of the composite SNTs was tested by the photodegradation of RhB dyes. Typically, 2 mg of as-prepared samples were added to 10 mL of RhB solution with a concentration of 10 mg·L^{-1}. Then, the suspension was placed in the dark for 30 min with gentle stirring in order to reach absorption equilibrium. Then, the mixed solutions were illuminated under a mercury and tungsten mixed light lamp (300 W, including the UV and visible light region for simulating the sunlight environment). The solutions were sampled at 15 min intervals, and the corresponding UV−vis spectra (measured in the range of 650 to 450 nm) were recorded to monitor the progress of the reaction by using a Shimadzu 2550 spectrophotometer.

RESULTS AND DISCUSSION

The formation of tube-like ternary α-Fe_2O_3@SnO_2@Cu_2O single core-double shell sandwich heterostructures involves a three-step process, and the schematic illustration of the formation process is described in Figure 1. First, monodisperse α-Fe_2O_3 SNTs were prepared using an anion-assisted hydrothermal route. Then, α-Fe_2O_3@SnO_2 composite SNTs with well-defined core−shell structures were obtained through the

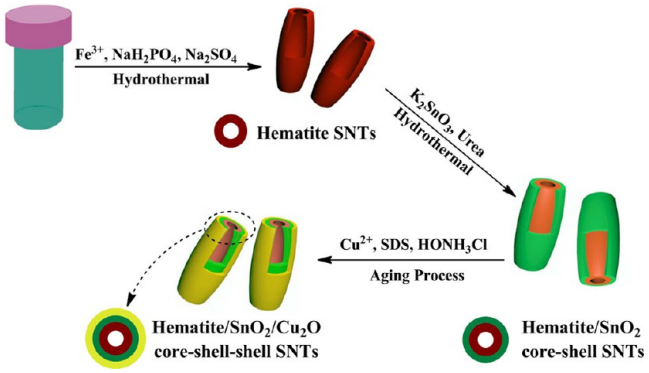

Figure 1. Schematic illustration of the formation process of α-Fe_2O_3@SnO_2@Cu_2O single core-double shell sandwich heterostructures.

seed-mediated deposition strategy in the presence of hematite seeds, and the average thickness of the shell coating was about 40 nm. Through the aging process, Cu_2O with different thicknesses were deposited on the surface of the α-Fe_2O_3@SnO_2 composite SNTs to get tube-like ternary α-Fe_2O_3@SnO_2@Cu_2O single core-double shell heterostructures. In this structure, the bandgaps of n-type α-Fe_2O_3, n-type SnO_2, and p-type Cu_2O are 2.3, 3.6, and 2.2 eV, respectively, and thus form a heterostructure with a narrow-wide bandgap composite system and p−n heterojunction system, which are beneficial to reduce the recombination of electron and hole pairs.

The detailed microstructural characterization of α-Fe_2O_3 seeds was performed by electron microscopy and XRD. As shown in Figure 2a, as-obtained α-Fe_2O_3 products exhibit tube-like shape, and the feature of end-opening for a tube can be clearly observed. Figure 2b shows the TEM image of the as-obtained α-Fe_2O_3 products, where the obvious electron-density differences between the dark edge and pale center further confirm the hollow short tubular structure. The average length, outer diameter, and tube-wall thickness of α-Fe_2O_3 SNTs are about 547, 237, and 20 nm, respectively. Figure 2c shows the HRTEM image of a single α-Fe_2O_3 SNT taken from the central region. The clear lattice image indicates the high crystallinity of α-Fe_2O_3 SNTs. The lattice spacing of 0.170, 0.220, and 0.228 nm for (116), (113), and (006) planes indicate the rhombohedral hematite structure. Subsequently, the structure and phase purity of as-obtained α-Fe_2O_3 SNTs were examined by XRD, as shown in Figure 2d, and all the peaks can be well indexed to a pure rhombohedral structure of hematite (JCPDS PDF 33-0664). The above results illustrate that the tube-like α-Fe_2O_3 seeds are obtained.

After being coated with a wide bandgap semiconductor of tin oxide via the seed-mediated hydrothermal route, uniform α-Fe_2O_3@SnO_2 core−shell SNTs are obtained. In comparison with naked α-Fe_2O_3 SNTs, the surface of SNTs becomes smooth due to the coating (Figure 3a). Figure 3b shows the TEM image of α-Fe_2O_3@SnO_2 core−shell SNTs. From the images, it is clear that hollow and tube-like features are still maintained after coating, and the average outer diameter increases to 300 nm, which reveals that the average thickness of the SnO_2 coating layer is 31.5 nm. There is no obvious contrast of the end-opening part of pure α-Fe_2O_3 SNTs, as shown in Figure S1 (see the Supporting Information); after the coating of SnO_2, we determine its thickness from the tube-wall region. The corresponding selected area electron diffraction (SAED) pattern further reveals the presence of SnO_2. TEM images

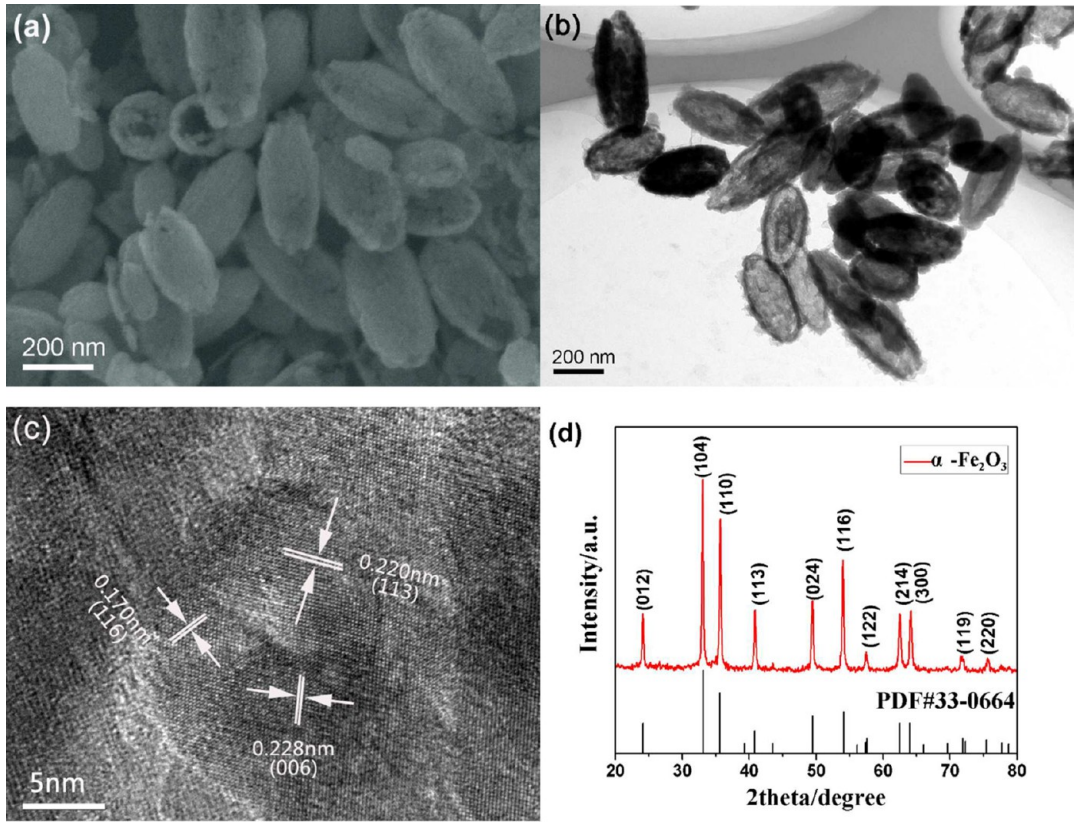

Figure 2. FESEM (a), TEM (b), HRTEM images (c, taken from the central region of the SNT), and XRD pattern (d) of as-prepared α-Fe_2O_3 SNTs.

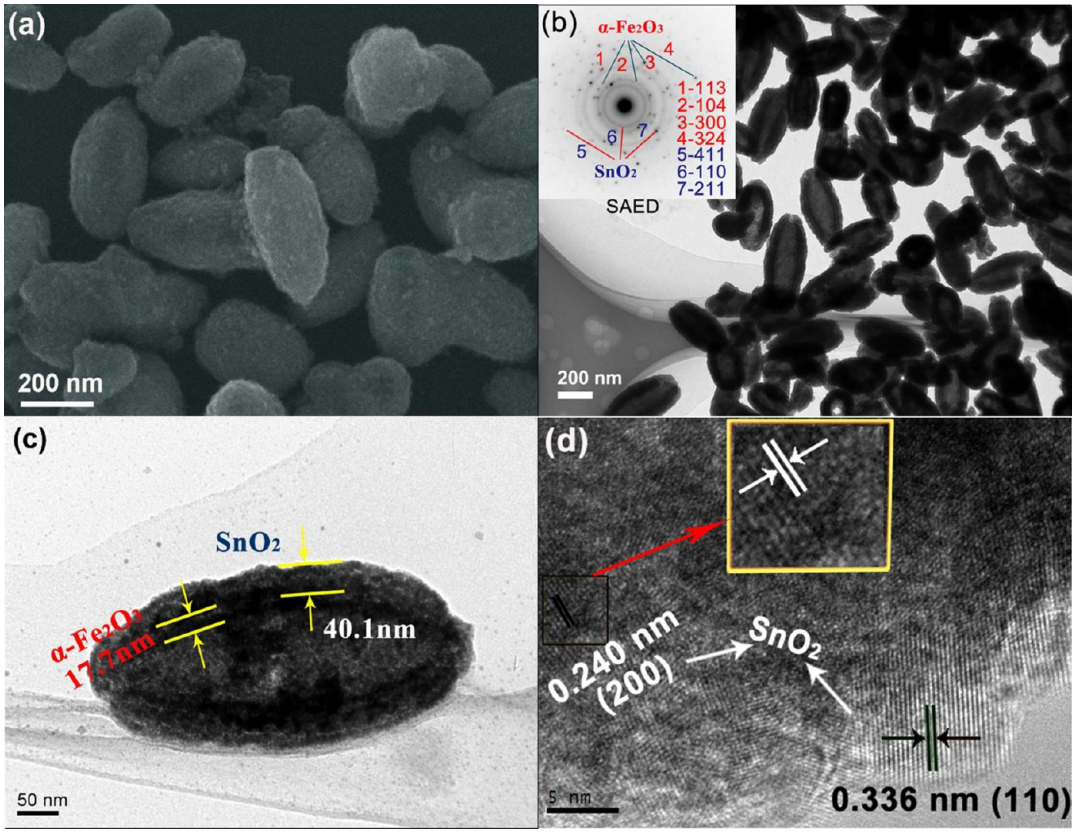

Figure 3. FESEM (a) and TEM images (b, the inset is the SAED pattern) of SnO_2 coated α-Fe_2O_3 SNTs, TEM image of an individual α-Fe_2O_3@SnO_2 core−shell heterostructure (c), and the corresponding HRTEM image take from the edge region (d).

(Figure 3c) of individual SNTs clearly reveal the obvious core−shell structure with a solid SnO_2 shell of 40.1 nm thickness (the measured values). The HRTEM image obviously reveals that the SnO_2 coating layer is well crystallized with a *d*-spacing of 0.240 and 0.336 nm, which can be matched to the d_{200} and d_{110} lattices, respectively. The above results demonstrate that α-Fe_2O_3@SnO_2 core−shell SNTs have been successfully fabricated by hydrothermal treatment. It is hard to avoid the growth of SnO_2 inside α-Fe_2O_3. However, the hollow short-tubular structure of α-Fe_2O_3@SnO_2 SNTs is well maintained, as can be seen from the TEM images.

Subsequently, the tube-like ternary α-Fe_2O_3@SnO_2@Cu_2O single core-double shell sandwich heterostructures with different thicknesses of Cu_2O shell have been prepared by the aging process. Figure 4 shows the XRD patterns of α-Fe_2O_3@SnO_2 binary SNTs and α-Fe_2O_3@SnO_2@Cu_2O ternary SNTs with different concentrations of Cu precursor, together with those of the standard JCPDS card of pure SnO_2 (41−1445, blue lines) and Cu_2O (05−0667, red lines) for comparison. As shown in curve a, besides the diffraction peaks of α-Fe_2O_3, the diffraction peaks of SnO_2 shells can be clearly identified from the pattern that could be indexed to (110), (101), and (211) planes of rutile phase of SnO_2.[27] The curves b, c, and d represent the XRD pattern of as-prepared α-Fe_2O_3@SnO_2@Cu_2O ternary SNTs with different concentrations of Cu precursor of 1, 50, and 100 mM, respectively. Obviously, the diffraction peaks of Cu_2O shells can be clearly identified from the pattern that could be indexed to (111), (200), and (220) planes of cubic phase of Cu_2O.[28] It is noteworthy that the intensity of diffraction peaks of Cu_2O increases along with the increasing Cu precursor concentration. No other additional peaks

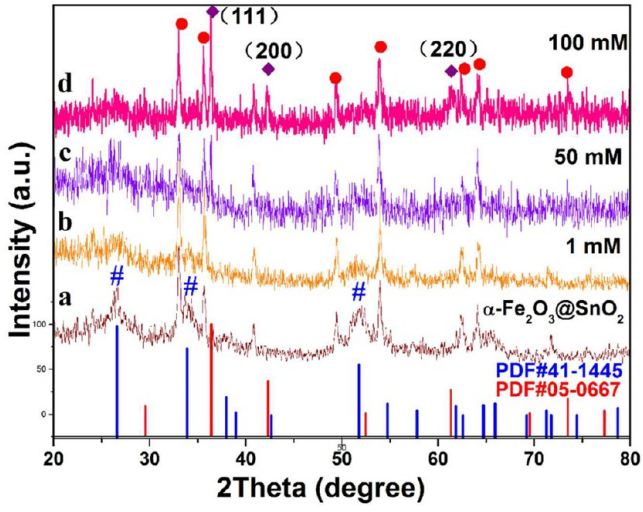

Figure 4. XRD pattern of α-Fe_2O_3@SnO_2 SNTs (curve a) and the as-obtained α-Fe_2O_3@SnO_2@Cu_2O with 1 mM (b), 50 mM (c), and 100 mM (d) of Cu precursor, together with those of standard JCPDS cards of pure SnO_2 (41−1445, blue lines) and Cu_2O (05−0667, red lines); the labeled #, ●, and ◆ represent the diffraction peaks of α-Fe_2O_3, SnO_2, and Cu_2O, respectively.

corresponding to impurities are found, indicating the purity of the sample.

The detailed morphology and microstructure of the α-Fe_2O_3@SnO_2@Cu_2O ternary heterostructures have been studied when the concentration of copper precursor is 1 mM (S1), as shown in Figure 5. As shown in Figure 5a, the

dx.doi.org/10.1021/am5029439 | ACS Appl. Mater. Interfaces 2014, 6, 13088−13097

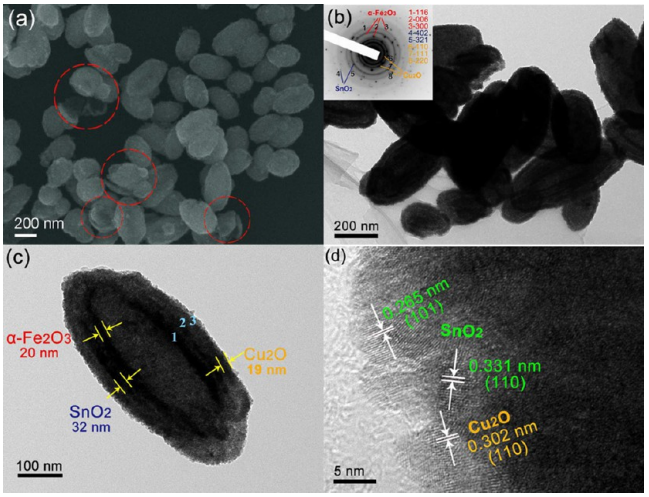

Figure 5. FESEM (a) and TEM images (b, the inset is the SAED pattern) of Cu_2O coated α-Fe_2O_3/SnO_2 core–shell SNTs ($C_{Cu\ precursor}$ = 1 mM) and TEM image of individual α-Fe_2O_3@SnO_2@Cu_2O single core-double shell heterostructure (c) and corresponding HRTEM image taken from the edge region (d).

morphology results from the smooth α-Fe_2O_3@SnO_2 binary SNTs indicate the uniform coating of numerous small Cu_2O nanoparticles. Incompletely coated SNTs can also be found in the product due to the low amount of Cu precursor used in the reaction. However, these incompletely-coated SNTs provide us with deep insights of the growth mechanism and elaborate the structural design of Cu_2O shell. In principle, the copper ions should all become $Cu(OH)_2$ colloidal particles before being reduced to form Cu_2O. The growth mechanism can be described as the hollow-shell-refilled (HSR) growth mechanism, in which the Cu_2O shells and the α-Fe_2O_3@SnO_2 binary SNTs are connected by Cu_2O bridges first and then completely filled by Cu_2O.[29] Figure 5b shows the TEM image of α-Fe_2O_3@SnO_2@Cu_2O ternary heterostructures; it can be seen that the hollow feature is still maintained after coating, and the average outer diameter continues to increase and reaches to 340 nm. As shown in Figure 5c, the clear interface of α-Fe_2O_3/SnO_2 and SnO_2/Cu_2O can be observed in the magnified TEM image of individual ternary SNTs. The thicknesses of the α-Fe_2O_3 SNT wall and SnO_2 and Cu_2O coating layers are 20, 31, and 19 nm, respectively. Figure 5d shows the HRTEM image of the labeled region from the individual ternary heterostructure. Interplanar spacing of 0.265, 0.331, and 0.302 nm can be indexed to the (110) and (101) planes of SnO_2 and (110) plane of Cu_2O, respectively. Those results reveal the successful formation of α-Fe_2O_3@SnO_2@Cu_2O ternary core–shell–shell structures by the present method.

In order to tailor the photocatalytic abilities, we adjust the concentration of copper precursor to 50 mM (S2) and 100 mM (S3), respectively, and the electron microscopy images of the as-obtained products are shown in Figure 6. When the concentration of copper precursor is increased, the α-Fe_2O_3/SnO_2 core–shell SNTs is found to be fully coated by the Cu_2O layer, as shown in Figure 6a,d. In addition, the obtained products exhibit an elliptical feature rather than the tube-like structures. In comparison with the bare α-Fe_2O_3/SnO_2 core–shell SNTs, the thickness of the as-grown Cu_2O layer is found to be 26 and 34 nm for S2 and S3, respectively. Figure 6b,e is the TEM image of S2 and S3, which reveal a sandwich structure of the composite heterostructures with a hollow α-Fe_2O_3 SNTs, a dark SnO_2 middle layer, and a light-dark Cu_2O shell. The clear observation of this unique structure is due to the distinct mass contrast between these three components. It is noteworthy to see few agglomerated Cu_2O nanoparticles in S3 (labeled), which explain the continuous increase of $CuCl_2$ amount leading to an increase of free Cu_2O nanoparticles. The inset SAED pattern shows spotty diffraction rings that could be indexed precisely to these three components with the polycrystalline feature. The interplanar spacing of 0.246 nm can be found in the HRTEM image of the surface of the α-Fe_2O_3@SnO_2@Cu_2O ternary heterostructure and can be indexed to the

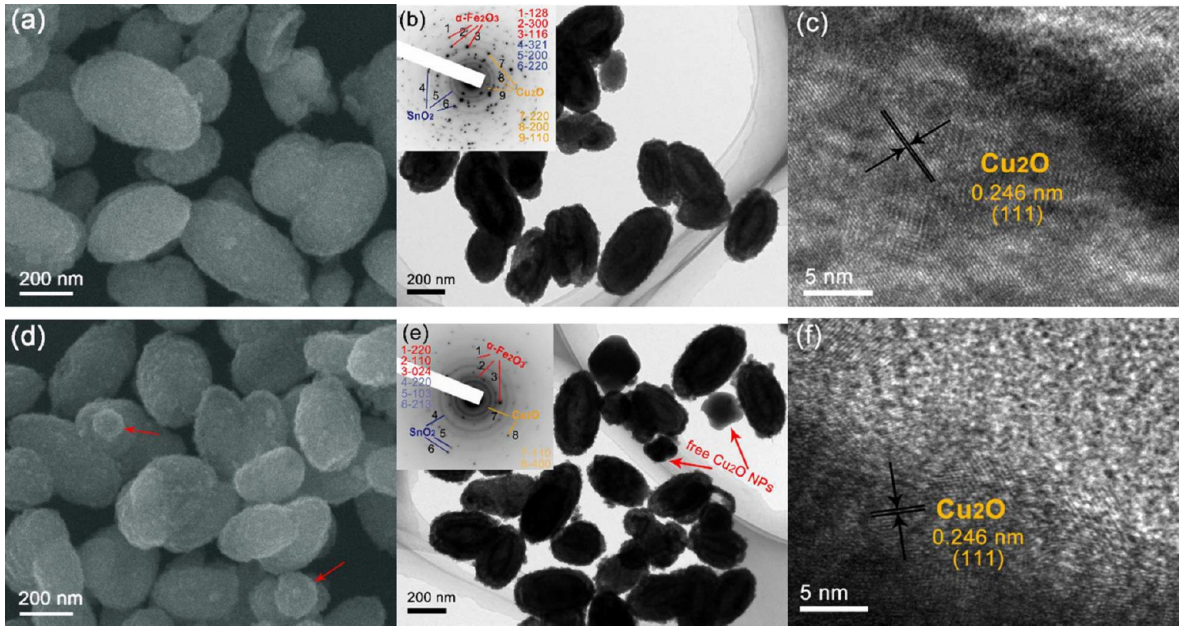

Figure 6. FESEM (a, d), TEM (b, e), and HRTEM (c, f) images of α-Fe_2O_3@SnO_2@Cu_2O single core-double shell heterostructures when the concentration of Cu precursor was elevated to 50 and 100 mM, respectively.

(111) plane of cuprite Cu_2O. In comparison with sample S1, no crystal palate of SnO_2 is detected, indicating that α-Fe_2O_3/SnO_2 core−shell SNTs have been fully coated by Cu_2O due to the increased concentration of copper precursor.

As shown in Figure 7, energy-dispersive X-ray (EDX) analysis was used to determine the change of Cu elemental

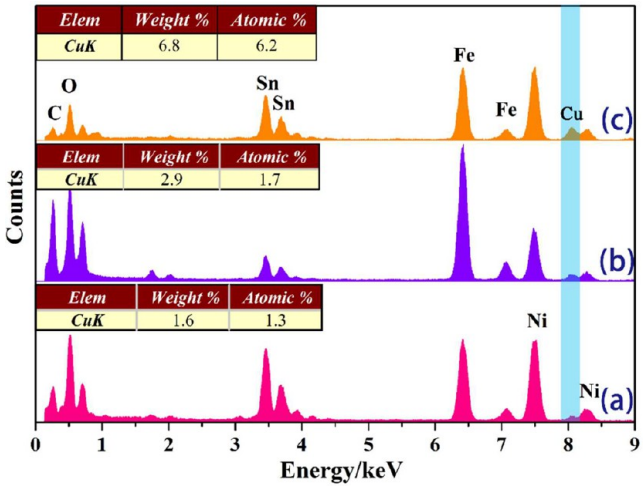

Figure 7. EDX spectrum of the as-obtained individual α-Fe_2O_3@SnO_2@Cu_2O single core-double shell heterostructure when the concentration of Cu precursor is 1 (a), 50 (b), and 100 mM (c), respectively.

composition of the individual α-Fe_2O_3@SnO_2@Cu_2O ternary single core-double shell heterostructure. The EDX spectra reveals the presence of Fe, Sn, Cu, and O elements (Ni element comes from the nickel grid) and illustrates the presence of Cu_2O on the α-Fe_2O_3@SnO_2 SNTs surface during the aging process. As shown in the inset table, the measured quantitative percentages of Cu in the as-prepared samples of $C_{cu\ precursor}$ at 1, 50, and 100 mM are 1.6, 2.9, and 6.8 wt %, respectively. Obviously, the weight percentage of Cu element increases with the increase in Cu precursor, which demonstrates that the Cu_2O layer could be tailored by the concentration of copper precursor.

The composition and element valence states of the samples were also investigated by XPS, and the results are showed in Figure 8. The full-scale XPS spectrum in Figure S2a (see the Supporting Information, Figure S2) reveals that the synthesized samples are composed of elements such as Fe, Sn, Cu, and O (a high concentration of C is found due to the binding energy (E_g) for C 1s (284.5 eV) as the internal reference). High-resolution XPS spectra of C 1s are shown in Figure S2b, Supporting Information; the main peaks at 285.5 and 284.0 eV belong to the characteristic C 1s peaks for the α-Fe_2O_3@SnO_2@Cu_2O single core-double shell sandwich heterostructures at $C_{Cu\ precursor}$ = 1 mM and $C_{Cu\ precursor}$ = 100 mM, between which a slight shift of ΔE_g = 1.5 eV should be responsible for the signal differentials of Cu and Sn elements (the element of C 1s is selected as the reference coordinate; see the Supporting Information). Figure 8a shows the high-resolution XPS scans over Sn 3d peaks. The main peaks located at ∼493.53 and ∼485.13 eV or ∼494.98 and ∼486.58 eV are attributed to the Sn $3d_{3/2}$ and Sn $3d_{5/2}$ binding energy of the $C_{Cu\ precursor}$ = 1 mM and $C_{Cu\ precursor}$ = 100 mM, respectively, which illustrate the existence of tin oxide. Interestingly, the intensity of Sn element (united by CPS) of α-Fe_2O_3@SnO_2@Cu_2O is obviously lower than that of α-Fe_2O_3@SnO_2 due to the shielding effect (or blocking effect) of XPS after the Cu_2O coating. Indeed, several reports demonstrate that, if particles possess a core and shell structure, the core is screened by the shell and the composition of the shell layer becomes gradually more dominant, and the intensity ratio of the shell/core spectra will gradually increase.[30−33] The XPS results indicate that the α-Fe_2O_3@SnO_2 core has been fully coated with the Cu_2O shell format, thus reducing the signal intensity of the inside element. The XPS spectrum of Cu 2p is shown in Figure 8b. It can be observed that two characteristic peaks arising from ∼951.38 and ∼932.13 eV or ∼952.68 and ∼933.43 eV corresponding to Cu $2p_{1/2}$ and Cu $2p_{3/2}$ orbitals of Cu^+, respectively, confirm the existence of Cu^+ on the sample surface. All the photoelectron signals of the two samples have a slight shift of 1.5 eV.

In order to evaluate the photocatalytic activities of as-synthesized α-Fe_2O_3@SnO_2@Cu_2O single core-double shell heterostructures, the photodegradation of RhB dye in water under UV and visible-mixed light irradiation (for simulating the sunlight environment) was carried out. Figure 9 shows the comparison of photocatalytic activity of as-obtained α-Fe_2O_3@SnO_2@Cu_2O ternary heterostructure samples with different concentrations of copper precursor, naked α-Fe_2O_3 seeds, and bare α-Fe_2O_3@SnO_2 core−shell structure. It is obvious that core−shell α-Fe_2O_3@SnO_2 SNTs (78.76% of RhB can be

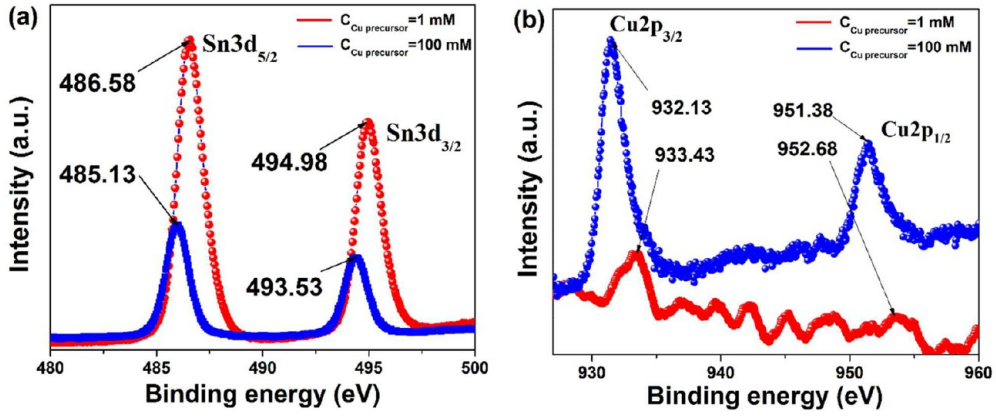

Figure 8. High-resolution XPS spectra of the tin Sn 4d peaks (a) and copper Cu 2p peaks (b) for the α-Fe_2O_3@SnO_2@Cu_2O single core-double shell sandwich heterostructure at $C_{Cu\ precursor}$ = 1 mM and $C_{Cu\ precursor}$ = 100 mM, respectively.

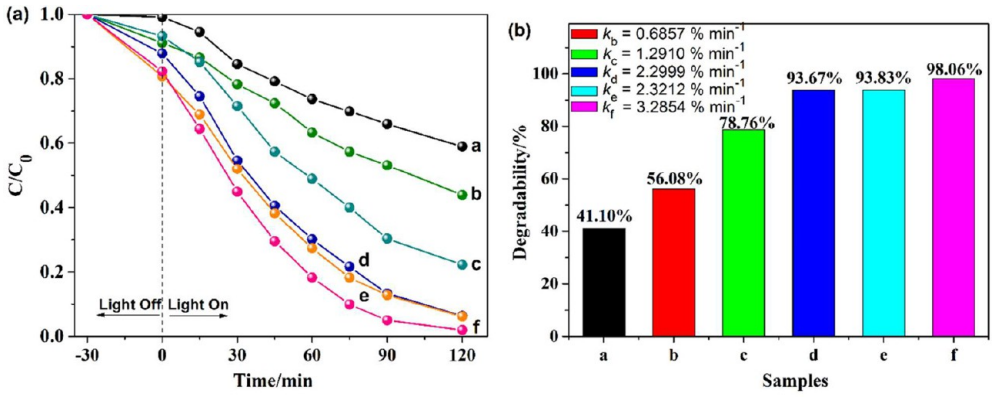

Figure 9. Photodegradation (a) and degradability distributions (b) of RhB by different catalysts under simulated sunlight irradiation for 120 min: bare (a), naked α-Fe_2O_3 SNTs (b), α-Fe_2O_3@SnO_2 core–shell heterostructures (c), and α-Fe_2O_3@SnO_2@Cu_2O single core-double shell sandwich heterostructures (d, $C_{Cu\ precursor}$ = 1 mM; e, $C_{Cu\ precursor}$ = 50 mM; f, $C_{Cu\ precursor}$ = 100 mM).

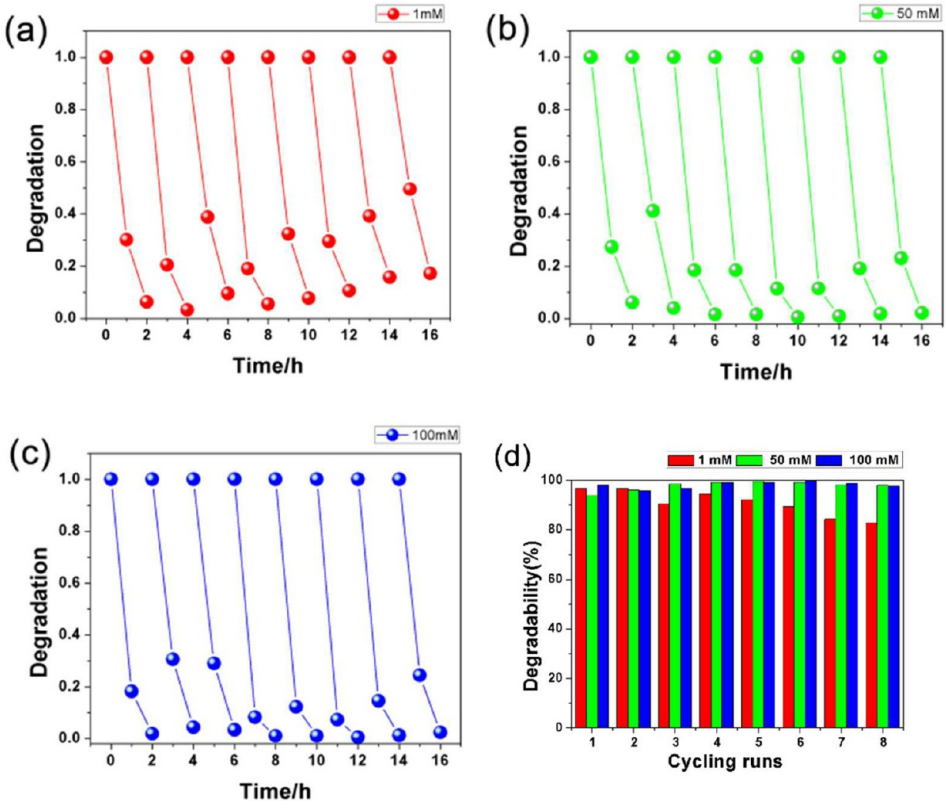

Figure 10. Degradability of different cycling runs for photocatalytic degradation of RhB in the presence of the as-obtained tube-like α-Fe_2O_3@SnO_2@Cu_2O samples of S1 (a), S2 (b), and S3 (c) and photocatalytic degradation rate at different recycling times (d).

degraded) show higher photocatalytic activity than α-Fe_2O_3 SNTs (56.08% of RhB can be degraded) under identical experimental conditions. The enhanced photocatalytic property of α-Fe_2O_3@SnO_2 SNTs can be attributed to the high separation rate of electrons and holes under the influence of the heterojunction between two different semiconductors possessing a narrow-wide band gap.[34] Another reason can be ascribed to the wide absorption band of the heterostructure covering almost all the UV–visible light spectra (see the Supporting Information, Figure S3). Although the absorbance of α-Fe_2O_3 in visible light is decreased due to the tin oxide coating, the fingerprint absorbance of α-Fe_2O_3 still could be observed in the UV–vis spectra (curve b, from 380 to 600 nm), and the results illustrate that Fe_2O_3 could absorb the visible light. In fact, the absorbance of tin oxide is in the UV range and the thickness (less than 40 nm) of SnO_2 cannot prevent the light from reaching the α-Fe_2O_3 layer. Furthermore, the RhB was almost completely degraded after 2 h of light irradiation with the ternary α-Fe_2O_3@SnO_2@Cu_2O core–shell–shell heterostructure (>90% of RhB is degraded) as the photocatalyst. After 2 h of irradiation, the maximum percentage of decomposed dye increases from 78% for bare α-Fe_2O_3@SnO_2 SNTs to 98% for α-Fe_2O_3@SnO_2@Cu_2O single core-double shell heterostructure ($C_{cu\ precursor}$ = 100 mM), as shown in Figure 9b (the absorption measurements for S1, S2, and S3 under a dark environment with gentle stirring for 2 h are shown in Figure S4, Supporting Information). The concentration of RhB for the three samples was decreased to 18.8%, 14.6%, and

dx.doi.org/10.1021/am5029439 | ACS Appl. Mater. Interfaces 2014, 6, 13088–13097

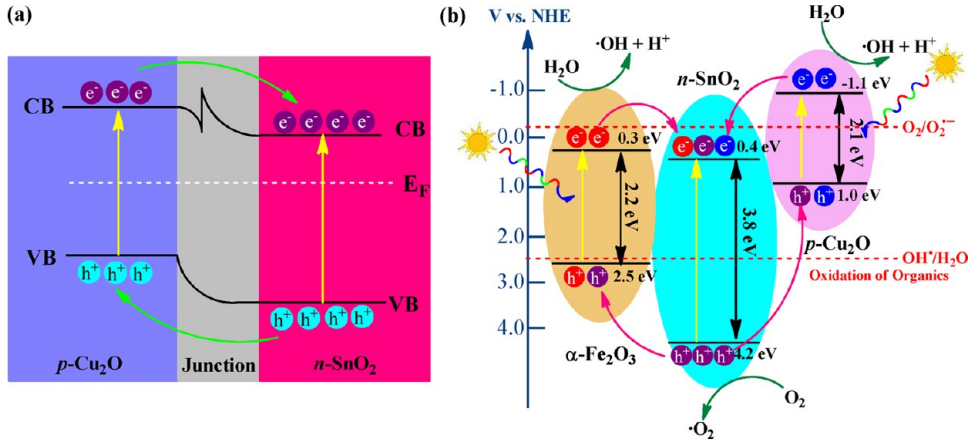

Figure 11. (a) Schematic illustration of the charge transfer process occurring at the Cu_2O/SnO_2 nanojunction under UV−visible light irradiation. (b) Schematic illustration of the valence and conduction band edges of α-Fe_2O_3, SnO_2 and Cu_2O.

27.9%, respectively, after 2 h under a dark environment. Therefore, the decrease of C/C_0 is due to the degradation and not the absorption. The kinetics of the degradation reaction are fitted to a pseudo first-order reaction at low dye concentrations: $-\ln(C/C_0) = kt$, where k is the apparent rate constant. The k value increases consistently from 0.0069 min^{-1} for naked α-Fe_2O_3 SNTs, to 0.0129 min^{-1} for bare α-Fe_2O_3@SnO_2 SNTs, and finally to 0.0329 min^{-1} for α-Fe_2O_3@SnO_2@Cu_2O single core-double shell heterostructure ($C_{cu\ precursor}$ = 100 mM). Remarkably high photocatalytic activity of ternary heterostructures could be explained by the hole-transfer mechanism of narrow and wide bandgap semiconductors and the p−n heterojunction.

Subsequently, the stability of photocatalyst of α-Fe_2O_3@SnO_2@Cu_2O core-double shell heterostructure has been further investigated by recycling the photocatalyst for RhB degradation (Figure 10). The heterostructure performed well with good photocatalytic activity; the degradation rate of RhB solution was found to be more than 85% after 8 cycles with duration of 120 min per cycle (S2 and S3 maintain the degradation rate of RhB solution at more than 95% after 8 cycles). The TEM images of samples after photocatalytic reaction have been added in the Supporting Information (Figure S5), which shows that the samples are stable after 8 cycles of degradation reaction. It is clear that photocatalytic efficiency does not exhibit significant loss after several recycles, indicating that the α-Fe_2O_3@SnO_2@Cu_2O core-double shell heterostructure has high stability and does not suffer from photocorrosion during the photocatalytic degradation of RhB.

In the current α-Fe_2O_3@SnO_2@Cu_2O single core-double shell heterostructural system, the SnO_2 and Cu_2O form the p−n heterojunction. This p−n heterojunction structure effectively suppresses the photogenerated electron−hole recombination that facilitates charge rectification and faster carrier migration.[35−37] As shown in Figure 11a, the band structures of Cu_2O and SnO_2 match well with each other, in which the conduction band (CB) edge of Cu_2O is higher than that of SnO_2, while the valence band (VB) edge of SnO_2 is lower than that of Cu_2O. Under UV−visible light irradiation, the electrons on the CB of Cu_2O quickly move to the CB of SnO_2, whereas the holes on the VB of SnO_2 transfer to the VB of Cu_2O, effectively realizing the charge separation process. More interestingly, a p−n junction effect exists at the interface region between the p-type Cu_2O and n-type SnO_2 in the Cu_2O/SnO_2 heterojunction further facilitating the charge transfer between Cu_2O and SnO_2.[38−40] As shown in Figures 3d, 5d, and 6c,f, the exposed crystal planes of SnO_2 are (200) and (110) with lattice spacing of 0.240 and 0.336 nm, respectively. The exposed crystal planes of Cu_2O are (111) and (110) with the lattice spacing of 0.246 and 0.302 nm, respectively. The (200) plane of SnO_2 has a lattice mismatch of 2.5% ($\delta = 2|d_1 - d_2|/(d_1 + d_2)$) with the (111) plane of Cu_2O, and the (110) plane of SnO_2 has a low lattice mismatch with the (110) plane of Cu_2O, by which the lattice mismatch degree is 10.66%. The low lattice mismatch is perfect and beneficial for the formation of the p−n heterojunction between Cu_2O and SnO_2. Additionally, on the basis of above experimental results, we draw a schematic illustration on the band structures of ternary heterostructures as shown in Figure 11b. Like the p−n junction, the conduction band (CB) edge of α-Fe_2O_3 is higher than that of SnO_2, while the valence band (VB) edge of SnO_2 is lower than that of α-Fe_2O_3; the band structures of α-Fe_2O_3 and SnO_2 match well with each other. In fact, this coupling of narrow band gap with the wide band gap semiconductor is beneficial to the separation of electron−hole pairs.[18] Under UV−visible light irradiation, the photogenerated electrons in the CB of α-Fe_2O_3 core tend to transfer to the CB of SnO_2 due to the driving force from the decreased potential energy. This core−shell heterostructure reduces the electron−hole recombination probability and enhances the electron mobility, and the photogenerated electrons and holes are separated at the α-Fe_2O_3/SnO_2 interface.[9,16,41,42] Therefore, the photogenerated electrons transfer to the surface of the SnO_2 interlayer in the current ternary core−shell−shell heterostructure, and the superoxygen radicals ($\cdot O_2$) are formed by the combination of electrons with O_2 adsorbed on the surface of SnO_2. Consequently, the holes are transferred to the surfaces of α-Fe_2O_3 and Cu_2O, respectively, and finally form hydroxyl radicals (·OH). As a powerful oxidant, the hydroxyl radicals effectively decompose the organic polluters such as RhB; eventually, the amount of Cu_2O affects the photocatalytic ability of ternary core−shell−shell heterostructure. Moreover, the incorporation of small band gap semiconductor, such as α-Fe_2O_3 and Cu_2O, increases the probability of absorption of radiation in the visible range that could be seen from the UV−visible spectrum. In our study, the thickness of SnO_2 was found to be 30 to 40 nm; if SnO_2 becomes thick, the heterostructure has an adverse effect on the photons penetration to α-Fe_2O_3. If SnO_2 is too thin, the

absorption of photon by SnO_2 would be low and influence the heterojunction formation as well. Therefore, our experiments are based on an average thickness of around 31.5 nm. Experiments are underway to understand the influence of the thickness of the SnO_2 interlayer on photocatalytic activity. Compared with the naked α-Fe_2O_3 SNTs and uncoated α-Fe_2O_3@SnO_2 core−shell SNTs, the enhanced photocatalytic performance of ternary core−shell−shell heterostructures is attributed to the effective separation of electron−hole pairs at the interface of α-Fe_2O_3/SnO_2 and SnO_2/Cu_2O. The broad solar spectral response (Figure S2, Supporting Information) enhances the concentration of electron−hole pairs, while the p−n heterostructure make the separation of charges efficiently. With the availability of more electrons and holes, the redox reactions can predominantly occur and eventually enhance the photocatalytic performance of the ternary heterostructured catalysts. Therefore, it is the synergistic effect of both aspects that contribute to the enhanced photocatalytic performance.

CONCLUSIONS

In summary, we have successfully prepared a tube-like ternary α-Fe_2O_3@SnO_2@Cu_2O single core-double shell heterostructure in a controlled way. The well designed ternary sandwich heterostructure facilitates the charge separation between the α-Fe_2O_3 and SnO_2 and the Cu_2O and SnO_2, while the tube-like hollow structure is beneficial for the dyes adsorption. These combined properties endow the α-Fe_2O_3@SnO_2@Cu_2O single core-double shell ternary heterostructure with enhanced photocatalytic performance for RhB dye degradation, which is better than that of bare α-Fe_2O_3 SNTs and α-Fe_2O_3@SnO_2 core−shell binary SNTs, respectively. This study demonstrates that the construction of composite heterostructure coupled with a heterojunction is an interesting strategy to enhance the photocatalytic activity of organic dyes decolorization. We anticipate that this unique concept could provide a versatile route to fabricate other heterostructural materials for higher solar-to-energy conversion efficiency.

ASSOCIATED CONTENT

Supporting Information

The full scan XPS spectra of samples S1 and S3, UV−vis absorption spectra of as-obtained samples, the absorption spectra of S1, S2, and S3 in the dark environment, and TEM images of as-obtained tube-like α-Fe_2O_3@SnO_2@Cu_2O samples after 8 cycles of photocatalytic degradation. This material is available free of charge via the Internet at http://pubs.acs.org.

AUTHOR INFORMATION

Corresponding Authors

*Tel: +86-27-68778529. Fax: +86-27-68778433. E-mail: weiwu@whu.edu.cn.
*E-mail: fren@whu.edu.cn.
*E-mail: val.roy@cityu.edu.hk.

Notes

The authors declare no competing financial interest.

ACKNOWLEDGMENTS

The authors thank Dr. Lixia Fan (Wuhan University of Science and Technology) for SEM analyses. This work was partially supported by the NSFC (51201115, 51171132, 11375134), Hong Kong Scholars Program, the Research Grants Council of the Hong Kong Special Administrative Region (Project No. T23-713/11), Young Chenguang Project of Wuhan City (2013070104010011), China Postdoctoral Science Foundation (2014M550406), and the Fundamental Research Funds for the Central Universities and Wuhan University.

REFERENCES

(1) Chaudhuri, G. R.; Paria, S. Core/Shell Nanoparticles: Classes, Properties, Synthesis Mechanisms, Characterization, and Applications. *Chem. Rev.* **2011**, *112*, 2373−2433.
(2) Schartl, W. Current Directions in Core-Shell Nanoparticle Design. *Nanoscale* **2010**, *2*, 829−843.
(3) Zhang, N.; Liu, S.; Xu, Y.-J. Recent Progress on Metal Core@Semiconductor Shell Nanocomposites as a Promising Type of Photocatalyst. *Nanoscale* **2012**, *4*, 2227−2238.
(4) Qu, Y.; Duan, X. Progress, Challenge and Perspective of Heterogeneous Photocatalysts. *Chem. Soc. Rev.* **2013**, *42*, 2568−2580.
(5) Kubacka, A.; Fernández-García, M.; Colón, G. Advanced Nanoarchitectures for Solar Photocatalytic Applications. *Chem. Rev.* **2011**, *112*, 1555−1614.
(6) Wu, W.; Xiao, X. H.; Zhang, S. F.; Ren, F.; Jiang, C. Z. Facile Method to Synthesize Magnetic Iron Oxides/TiO_2 Hybrid Nanoparticles and Their Photodegradation Application of Methylene Blue. *Nanoscale Res. Lett.* **2011**, *6*, 533.
(7) Mou, F.; Xu, L.; Ma, H.; Guan, J.; Chen, D.-r.; Wang, S. Facile Preparation of Magnetic γ-Fe_2O_3/TiO_2 Janus Hollow Bowls with Efficient Visible-Light Photocatalytic Activities by Asymmetric Shrinkage. *Nanoscale* **2012**, *4*, 4650−4657.
(8) Liu, S.; Zhang, N.; Tang, Z.-R.; Xu, Y.-J. Synthesis of One-Dimensional CdS@TiO_2 Core−Shell Nanocomposites Photocatalyst for Selective Redox: The Dual Role of TiO_2 Shell. *ACS Appl. Mater. Interfaces* **2012**, *4*, 6378−6385.
(9) Sun, L. L.; Wu, W.; Yang, S. L.; Zhou, J.; Hong, M. Q.; Xiao, X. H.; Ren, F.; Jiang, C. Z. Template and Silica Interlayer Tailorable Synthesis of Spindle-Like Multilayer α-Fe_2O_3/Ag/SnO_2 Ternary Hybrid Architectures and Their Enhanced Photocatalytic Activity. *ACS Appl. Mater. Interfaces* **2014**, *6*, 1113−1124.
(10) Wu, W.; Zhang, S. F.; Ren, F.; Xiao, X. H.; Zhou, J.; Jiang, C. Z. Controlled Synthesis of Magnetic Iron Oxides@SnO_2 Quasi-Hollow Core-Shell Heterostructures: Formation Mechanism, and Enhanced Photocatalytic Activity. *Nanoscale* **2011**, *3*, 4676−4684.
(11) Zhou, W.; Cheng, C.; Liu, J.; Tay, Y. Y.; Jiang, J.; Jia, X.; Zhang, J.; Gong, H.; Hng, H. H.; Yu, T.; Fan, H. J. Epitaxial Growth of Branched α-Fe_2O_3/SnO_2 Nano-Heterostructures with Improved Lithium-Ion Battery Performance. *Adv. Funct. Mater.* **2011**, *21*, 2439−2445.
(12) Zhu, L.-P.; Bing, N.-C.; Yang, D.-D.; Yang, Y.; Liao, G.-H.; Wang, L.-J. Synthesis and Photocatalytic Properties of Core-Shell Structured α-Fe_2O_3@SnO_2 Shuttle-Like Nanocomposites. *CrystEngComm* **2011**, *13*, 4486−4490.
(13) Xu, J.; Huang, F.; Yu, Y.; Yang, A.; Wang, Y. SnO_2/α-Fe_2O_3 Nanoheterostructure with Novel Architecture: Structural Characteristics and Photocatalytic Properties. *CrystEngComm* **2011**, *13*, 4873−4877.
(14) Li, Y.; Hu, Y.; Jiang, H.; Hou, X.; Li, C. Phase-Segregation Induced Growth of Core-Shell α-Fe_2O_3/SnO_2 Heterostructures for Lithium-Ion Battery. *CrystEngComm* **2013**, *15*, 6715−6721.
(15) Kang, J.; Kuang, Q.; Xie, Z.-X.; Zheng, L.-S. Fabrication of the SnO_2/α-Fe_2O_3 Hierarchical Heterostructure and Its Enhanced Photocatalytic Property. *J. Phys. Chem. C* **2011**, *115*, 7874−7879.
(16) Wu, W.; Zhang, S. F.; Xiao, X. H.; Zhou, J.; Ren, F.; Sun, L. L.; Jiang, C. Z. Controllable Synthesis, Magnetic Properties, and Enhanced Photocatalytic Activity of Spindlelike Mesoporous α-Fe_2O_3/ZnO Core-Shell Heterostructures. *ACS Appl. Mater. Interfaces* **2012**, *4*, 3602−3609.
(17) Li, X.; Huang, R.; Hu, Y.; Chen, Y.; Liu, W.; Yuan, R.; Li, Z. A Templated Method to Bi_2WO_6 Hollow Microspheres and Their Conversion to Double-Shell Bi_2O_3/Bi_2WO_6 Hollow Microspheres

with Improved Photocatalytic Performance. *Inorg. Chem.* **2012**, *51*, 6245−6250.
(18) Vinu, R.; Madras, G. Environmental Remediation by Photocatalysis. *J. Indian Inst. Sci.* **2010**, *90*, 189−230.
(19) Ida, S.; Takashiba, A.; Koga, S.; Hagiwara, H.; Ishihara, T. Potential Gradient and Photocatalytic Activity of an Ultrathin p−n Junction Surface Prepared with Two-Dimensional Semiconducting Nanocrystals. *J. Am. Chem. Soc.* **2014**, *136*, 1872−1878.
(20) He, Z.; Shi, Y.; Gao, C.; Wen, L.; Chen, J.; Song, S. BiOCl/$BiVO_4$ p−n Heterojunction with Enhanced Photocatalytic Activity under Visible-Light Irradiation. *J. Phys. Chem. C* **2013**, *118*, 389−398.
(21) Zhang, Z.; Shao, C.; Li, X.; Wang, C.; Zhang, M.; Liu, Y. Electrospun Nanofibers of p-Type NiO/n-Type ZnO Heterojunctions with Enhanced Photocatalytic Activity. *ACS Appl. Mater. Interfaces* **2010**, *2*, 2915−2923.
(22) Jiang, D.; Chen, L.; Zhu, J.; Chen, M.; Shi, W.; Xie, J. Novel p−n Heterojunction Photocatalyst Constructed by Porous Graphite-Like C_3N_4 and Nanostructured BIOI: Facile Synthesis and Enhanced Photocatalytic Activity. *Dalton Trans.* **2013**, *42*, 15726−15734.
(23) Zhao, W.-W.; Liu, Z.; Shan, S.; Zhang, W.-W.; Wang, J.; Ma, Z.-Y.; Xu, J.-J.; Chen, H.-Y. Bismuthoxyiodide Nanoflakes/Titania Nanotubes Arrayed pn Heterojunction and Its Application for Photoelectrochemical Bioanalysis. *Sci. Rep.* **2014**, *4*, 4426.
(24) Ganguli, A.; Basu, M.; Garg, N. A Type-II Semiconductor (ZnO/CuS Heterostructure) for Visible Light Photocatalysis. *J. Mater. Chem. A* **2014**, *2*, 7517−7525.
(25) Wu, W.; Xiao, X. H.; Zhang, S. F.; Zhou, J. A.; Fan, L. X.; Ren, F.; Jiang, C. Z. Large-Scale and Controlled Synthesis of Iron Oxide Magnetic Short Nanotubes: Shape Evolution, Growth Mechanism, and Magnetic Properties. *J. Phys. Chem. C* **2010**, *114*, 16092−16103.
(26) Wu, W.; Xiao, X. H.; Zhang, S. F.; Peng, T. C.; Zhou, J.; Ren, F.; Jiang, C. Z. Synthesis and Magnetic Properties of Maghemite (γ-Fe_2O_3) Short-Nanotubes. *Nanoscale Res. Lett.* **2010**, *5*, 1474−1479.
(27) Wu, W.; Zhang, S. F.; Zhou, J.; Xiao, X. H.; Ren, F.; Jiang, C. Z. Controlled Synthesis of Monodisperse Sub-100 nm Hollow SnO_2 Nanospheres: A Template- and Surfactant-Free Solution-Phase Route, the Growth Mechanism, Optical Properties, and Application as a Photocatalyst. *Chem.—Eur. J.* **2011**, *17*, 9708−9719.
(28) Hung, L. I.; Tsung, C. K.; Huang, W.; Yang, P. Room-Temperature Formation of Hollow Cu_2O Nanoparticles. *Adv. Mater.* **2010**, *22*, 1910−1914.
(29) Kuo, C.-H.; Hua, T.-E.; Huang, M. H. Au Nanocrystal-Directed Growth of Au-Cu_2O Core−Shell Heterostructures with Precise Morphological Control. *J. Am. Chem. Soc.* **2009**, *131*, 17871−17878.
(30) Liu, S.; Ma, Y.; Armes, S. P.; Perruchot, C.; Watts, J. F. Direct Verification of the Core−Shell Structure of Shell Cross-Linked Micelles in the Solid State Using X-ray Photoelectron Spectroscopy. *Langmuir* **2002**, *18*, 7780−7784.
(31) Yonezawa, T.; Toshima, N. Mechanistic Consideration of Formation of Polymer-Protected Nanoscopic Bimetallic Clusters. *J. Chem. Soc., Faraday Trans.* **1995**, *91*, 4111−4119.
(32) Remita, H.; Etcheberry, A.; Belloni, J. Dose Rate Effect on Bimetallic Gold-Palladium Cluster Structure. *J. Phys. Chem. B* **2003**, *107*, 31−36.
(33) Lu, L.; Sun, G.; Zhang, H.; Wang, H.; Xi, S.; Hu, J.; Tian, Z.; Chen, R. Fabrication of Core-Shell Au-Pt Nanoparticle Film and Its Potential Application as Catalysis and SERS Substrate. *J. Mater. Chem.* **2004**, *14*, 1005−1009.
(34) Rawal, S. B.; Bera, S.; Lee, D.; Jang, D.-J.; Lee, W. I. Design of Visible-Light Photocatalysts by Coupling of Narrow Bandgap Semiconductors and TiO_2: Effect of Their Relative Energy Band Positions on the Photocatalytic Efficiency. *Catal. Sci. Technol.* **2013**, *3*, 1822−1830.
(35) Xi, G.; Ouyang, S.; Ye, J. General Synthesis of Hybrid TiO_2 Mesoporous "French Fries" Toward Improved Photocatalytic Conversion of CO_2 into Hydrocarbon Fuel: A Case of TiO_2/ZnO. *Chem.—Eur. J.* **2011**, *17*, 9057−9061.
(36) Yao, W.; Zhang, B.; Huang, C.; Ma, C.; Song, X.; Xu, Q. Synthesis and Characterization of High Efficiency and Stable Ag_3PO_4/TiO_2 Visible Light Photocatalyst for the Degradation of Methylene Blue and Rhodamine B Solutions. *J. Mater. Chem.* **2012**, *22*, 4050−4055.
(37) Hua, X.; Shuxin, O.; Lequan, L.; Defa, W.; Tetsuya, K.; Jinhua, Y. Porous-Structured Cu_2O/TiO_2 Nanojunction Material Toward Efficient CO_2 Photoreduction. *Nanotechnology* **2014**, *25*, 165402.
(38) Deo, M.; Shinde, D.; Yengantiwar, A.; Jog, J.; Hannoyer, B.; Sauvage, X.; More, M.; Ogale, S. Cu_2O/ZnO Hetero-Nanobrush: Hierarchical Assembly, Field Emission and Photocatalytic Properties. *J. Mater. Chem.* **2012**, *22*, 17055−17062.
(39) Lin, J.; Shen, J.; Wang, R.; Cui, J.; Zhou, W.; Hu, P.; Liu, D.; Liu, H.; Wang, J.; Boughton, R. I.; Yue, Y. Nano-p−n Junctions on Surface-Coarsened TiO_2 Nanobelts with Enhanced Photocatalytic Activity. *J. Mater. Chem.* **2011**, *21*, 5106−5113.
(40) Cui, G.; Zhang, M.; Zou, G. Resonant Tunneling Modulation in Quasi-2D Cu_2O/SnO_2 pn Horizontal-Multi-Layer Heterostructure for Room Temperature H_2S Sensor Application. *Sci. Rep.* **2013**, *3*, 1250.
(41) Niu, M. T.; Huang, F.; Cui, L. F.; Huang, P.; Yu, Y. L.; Wang, Y. S. Hydrothermal Synthesis, Structural Characteristics, and Enhanced Photocatalysis of SnO_2/α-Fe_2O_3 Semiconductor Nanoheterostructures. *ACS Nano* **2010**, *4*, 681−688.
(42) Zhang, S. F.; Ren, F.; Wu, W.; Zhou, J.; Xiao, X. H.; Sun, L. L.; Liu, Y.; Jiang, C. Z. Controllable Synthesis of Recyclable Core-Shell γ-Fe_2O_3@SnO_2 Hollow Nanoparticles with Enhanced Photocatalytic and Gas Sensing Properties. *Phys. Chem. Chem. Phys.* **2013**, *15*, 8228−8236.